CHEMISTRY OF MATERIALS
Cite This: Chem. Mater. XXXX, XXX, XXX−XXX
Article
pubs.acs.org/cm

Revealing the Chemical Mechanism of NaO_2 Decomposition by In Situ Raman Imaging

Hossein Yadegari, Mohammad Norouzi Banis, Xiaoting Lin, Alicia Koo, Ruying Li, and Xueliang Sun*

Department of Mechanical and Materials Engineering, University of Western Ontario, London, Ontario N6A 5B9, Canada

Supporting Information

ABSTRACT: Sodium−oxygen ($Na-O_2$) batteries exhibit a low charging overpotential owing to the reversible formation and decomposition of sodium superoxide (NaO_2) on discharge and charge cycles. However, the cycling performance of the battery system is compromised by the side reactions occurring between the reactive NaO_2 discharge product with the other components of the cell including the air electrode and the organic electrolyte. In the present study, we employ a Raman imaging technique to reveal the chemical mechanism behind the decomposition reaction of NaO_2 in the presence of diglyme-based electrolyte. Our results illustrate the formation of oxalate-based side products resulting from prolonged exposure of NaO_2 to the cell electrolyte. Moreover, we show that $Na_2O_2{\cdot}2H_2O$ is not the thermodynamically favorable side product for decomposition of NaO_2 and may only be formed under the high-energy beam used by the measuring probe. The findings of this study help to better understand the underlying chemical reaction mechanisms of $Na-O_2$ cells.

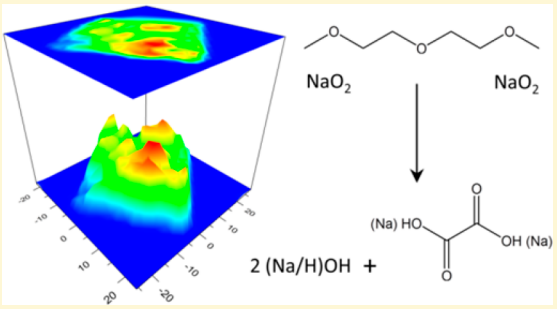

Considered as the next generation of the electrical energy storage systems, alkali metal-O_2 ($Li/Na-O_2$) cells provide the highest energy densities among all the available batteries.[1−4] However, the poor cycling performance of alkali metal−O_2 batteries hinders their development. The poor cycling performance in these batteries generally originates from instability of cell components against the highly oxidative environment in the cells. Moreover, the high charging overpotential associated with $Li-O_2$ cells triggers more parasitic side reactions which in turn compromise the cycling performance of the battery.[5,6] $Na-O_2$ cells, on the other hand, exhibit a low charging overpotential owing to the reversible formation and decomposition of NaO_2 on discharge and charge, respectively.[7] In addition, fewer side products were found to form during the electrochemical reaction of $Na-O_2$ cells compared to $Li-O_2$.[8] Nonetheless, $Na-O_2$ cells also display increased charging overpotential over cycling as well as short cycle life.[9]

Despite the similar nature of the oxygen reduction and evolution reactions (ORR and OER) occurring in $Li-O_2$ and $Na-O_2$ cells, the reaction mechanisms are not the same. The initially formed superoxide (O_2^-) ions in $Li-O_2$ cells chemically react with the cell electrolyte and carbonaceous air electrode, resulting in the formation of side products alongside Li_2O_2 discharge products.[5] In contrast, O_2^- ions can be stabilized in the presence of Na^+ ions with larger ionic radii to produce solid NaO_2 as the major discharge product in $Na-O_2$ cells.[7,8] Nevertheless, the produced NaO_2 is not thoroughly stable against the cell components and thus compromises the cycling performance of the battery.[9] Meanwhile, the side reactions involving metallic Na are partially accountable for the poor cycling performance of the batteries.[10] Accordingly, protection of metallic Na has been the subject of multiple recent studies.[11,12]

Instability of NaO_2 discharge products of the cells has been reported by a number of studies.[13−16] Moreover, we observed that NaO_2 gradually decomposes in the presence of a carbonaceous air electrode using in-line XRD measurements,[17] though the decomposition mechanism of NaO_2 is not yet clear. In the present study, we employ Raman spectroscopy to illustrate the mechanism behind the decomposition of the electrochemically formed NaO_2 in the $Na-O_2$ cell environment. We reveal the role of carbon electrodes as well as the ether-based electrolyte in the formation of the side products by monitoring the chemical changes associated with individual NaO_2 cubes in the actual cell environment.

Raman spectroscopy uses the visible region of the electromagnetic spectrum with low energy to excite the materials under study, hence minimizing the potential beam damage from the spectroscopic technique during the experiment. In addition, Raman spectroscopy provides high sensitivity and selectivity toward the discharge product and side products that form in $Na-O_2$ cells. We combine the visual data obtained from the optical microscope with Raman chemical information to elucidate the chemical decomposition reactions occurring in the cell. To monitor the chemical

Received: April 24, 2018
Revised: July 1, 2018
Published: July 2, 2018

DOI: 10.1021/acs.chemmater.8b01704
Chem. Mater. XXXX, XXX, XXX−XXX

changes of NaO_2 in the cell environment, a fully discharged air electrode was transferred into an airtight Raman cell and an individual NaO_2 cube was identified using the optical microscope. A typical optical image of the NaO_2 product obtained from the Raman microscope is presented alongside with a SEM image recorded using a similarly prepared sample in Figure S1 in Supporting Information for comparison purposes. Then, the NaO_2 cube was linearly scanned and Raman spectra were collected in an area of approximately 40 μm × 40 μm for 20 points in each X and Y direction (400 points in total). The obtained spectra were used to reproduce the chemical maps for different detected compounds. To monitor the chemical changes of NaO_2 in the cell environment, the described procedure was repeated for freshly prepared samples with and without added electrolyte over a prolonged period of 170 h.

Figure S2 compares the actual Raman spectra obtained from a linear scan on the samples at different time intervals. The spectra exhibit major peaks at 1156 cm^{-1}, related to the O−O stretching mode in NaO_2.[3] The intensity of the NaO_2 characteristic peak decreases over time for both samples, and a peak starts to rise at 1136 cm^{-1}. Besides, new peaks can be identified at 765, 860, and 1050 cm^{-1} in the case of the sample without added electrolyte. The decomposition reaction of NaO_2 occurs much faster in the presence of the cell electrolyte with no detectable superoxide after 150 h. The intensity of the Raman peaks was applied to reproduce the chemical maps at various wavenumbers during the experiment. The obtained maps for the dry discharged electrode are presented in Figures 1 and S3 for different frequencies. NaO_2 chemical maps exhibit a descending trend in peak intensity. However, the chemical maps at 1136 and 860 cm^{-1} display a mild enriching trend during the first 100 h and remain almost unchanged afterward.

Appearance of the Raman peak at 1136 cm^{-1} has been previously reported for the electrochemically formed NaO_2 subjected to aging in the cell or exposure to ambient air.[18,19] The peak at 1136 cm^{-1} has been attributed to the formation of $Na_2O_2{\cdot}2H_2O$. However, Na_2O_2 exhibits a pair of peaks at 738 and 793 cm^{-1} corresponding to the O−O stretching mode of O_2^{2-} in C_{3h} and D_{3h} sites (Figure S4).[20] The characteristic peaks of peroxide do not appear on the Raman spectra which contradict with the formation of Na_2O_2. Accordingly, appearance of the peak at 1136 cm^{-1} can be correlated to the O−O stretching mode of O_2^- with increased bond length due to the "solvent effect" caused by the surrounding matrix.[21,22] The nature of the peak at 1136 cm^{-1} will be discussed more in the following sections.

The Raman peak appearing at 1050 cm^{-1} can be related to the symmetric stretching modes of C−O and S−O in sodium bicarbonate ($NaHCO_3$) and sodium triflate ($NaCF_3SO_3$), respectively.[23,24] The Raman spectra of the corresponding standard compounds are also presented in Figure S5 for comparison. The two compounds, however, can be distinguished by the additional $NaCF_3SO_3$ peak at 765 cm^{-1} which is related to the symmetric stretching mode of C−S.[24] The chemical maps obtained at 1050 and 765 cm^{-1} (Figure S3) present similar features, suggesting the correlation between the two peaks. In addition, the maps obtained from dividing the peak intensity at 765 cm^{-1} by those of at 1050 and 860 cm^{-1} are depicted in Figure S6. The maps indicate that the peaks at 765 and 1050 cm^{-1} are correlated, confirming that the peak at 1050 cm^{-1} mainly results from the electrolyte salt precipitating on the electrode surface after drying the solvent, whereas the

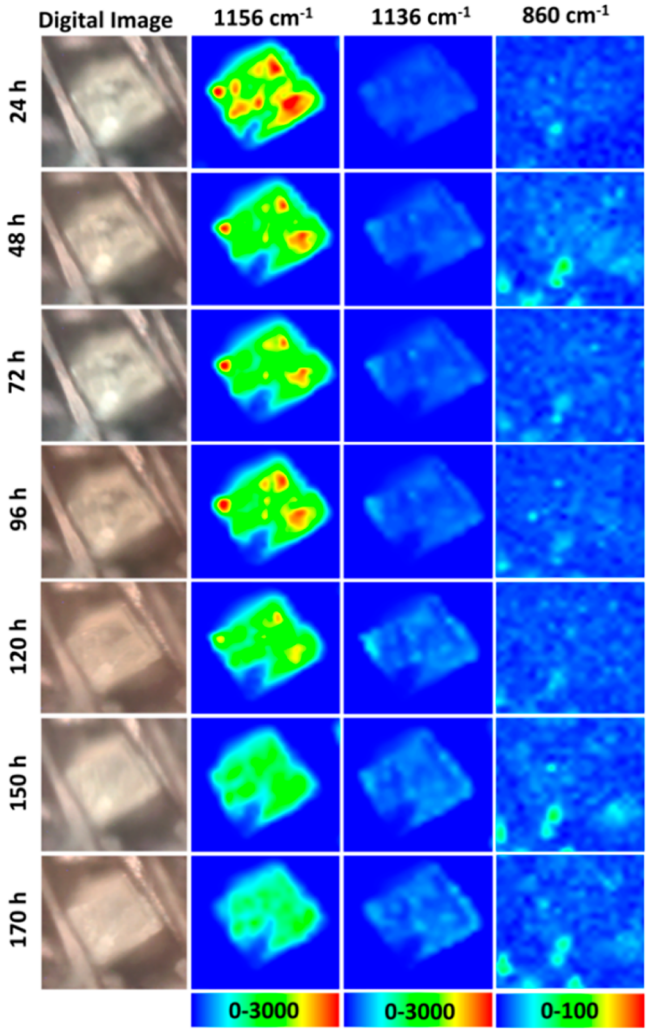

Figure 1. Chemical maps at various frequencies reproduced from Raman spectra recorded for a NaO_2 cube on a dry air electrode at different time intervals.

peak at 860 cm^{-1} is not correlated to the electrolyte salt despite the similarity of the resultant chemical maps. Nonetheless, overlaying the obtained chemical maps at 860 and 1050 cm^{-1} (Figure 2) illustrates that the corresponding side product is most likely from the reaction between the cell electrolyte and NaO_2.

To confirm the role of cell electrolyte in the formation of side products, the chemical composition of NaO_2 was monitored in the presence of added electrolyte. The obtained chemical maps in the presence of the additional electrolyte are depicted in Figures 3 and S7 for different frequencies. Chemical maps of NaO_2 demonstrate a much faster decomposition rate in the presence of the cell electrolyte; no superoxide can be detected after 150 h. Meanwhile, the chemical maps at 1136 cm^{-1} depict an increasing trend during the first 100 h and show a descending trend afterward. The chemical maps obtained at 860 cm^{-1}, however, display a constant formation of the side products which completely cover the NaO_2 surface after 170 h. Another notable change in the presence of the cell electrolyte is detection of $NaHCO_3$ throughout the experiment. As shown in Figure S7, most area on the chemical maps obtained at 1050 cm^{-1} can be related to $NaHCO_3$ in the absence of the characteristic peak for the

DOI: 10.1021/acs.chemmater.8b01704
Chem. Mater. XXXX, XXX, XXX−XXX

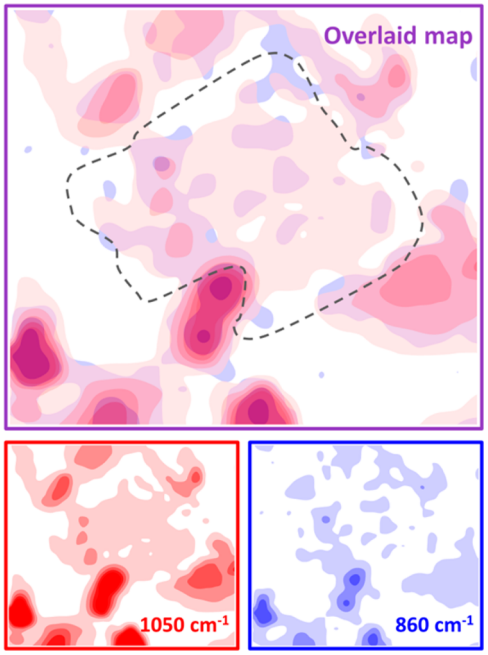

Figure 2. Chemical maps obtained by overlaying the Raman peaks at 860 and 1050 cm^{-1}. The dotted line determines the NaO_2 position.

electrolyte salt at 765 cm^{-1}. Furthermore, comparison of the chemical maps obtained for $NaHCO_3$ and carbon (1580 cm^{-1}) indicates that $NaHCO_3$ is mainly formed on the air electrode (Figure S8).

Carbonate-based side products were found on the air electrode around multiple NaO_2 cubes in a fresh discharged sample (Figure S9). Therefore, formation of sodium carbonate or bicarbonate can be related to the oxidation of the defect sites at the surface of the carbonaceous air electrode by superoxide ion upon discharge:[9,17]

$$=COH + O_2^- + Na^+ \rightarrow NaHCO_3 \quad (1)$$

$$-COOH + 2O_2^- + 2Na^+ \rightarrow Na_2CO_3 + O_2 + -OH \quad (2)$$

The amount of the carbonate-based side products (1050 cm^{-1}) does not show a significant change during the rest time (Figure S7). However, the side products are more uniformly distributed throughout the mapping area after 170 h which is likely due to the partial dissolution of the carbonates in the cell electrolyte and redeposition on the electrode surface.

As shown in Figure 3, the major side product resulting from the reaction between NaO_2 with the cell electrolyte exhibits a peak at 860−870 cm^{-1}. In addition, the peak at 860 cm^{-1} is also accompanied by the appearance of a broad feature centered at 1460 cm^{-1} (Figure S10). However, the latter peak is partially overlapped by the broad D- and G-band of carbon at 1350 and 1580 cm^{-1}. A corrected map was obtained by subtracting the average of the carbon peaks from the chemical map obtained at 1460 cm^{-1} (Figure S11). The resultant map is comparable with that obtained at 860 cm^{-1}. Meanwhile, the peaks at 860 and 1460 cm^{-1} can be correlated to the C−C and O−C=O stretching modes in oxalic acid ($H_2C_2O_4$) and sodium oxalate ($Na_2C_2O_4$), respectively (see also Figure S5).[25,26] Accordingly, a mixed phase of $(H/Na)_2C_2O_4$ is most likely formed following the decomposition reaction of the cell electrolyte on the NaO_2 surface. A reaction pathway based

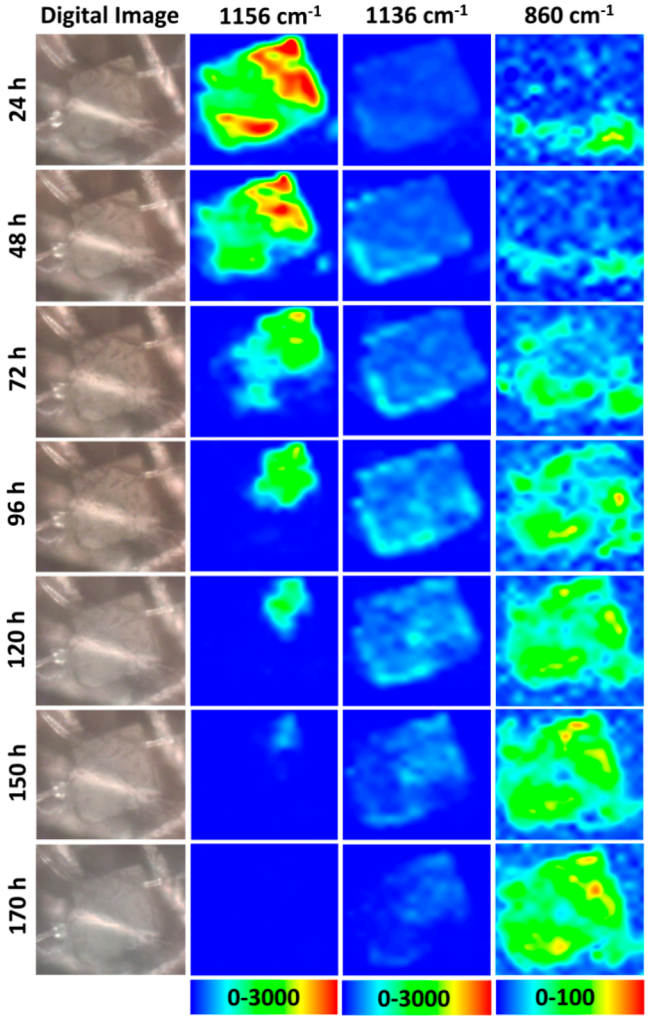

Figure 3. Chemical maps at various frequencies reproduced from Raman spectra recorded for a NaO_2 cube on an air electrode containing additional electrolyte at different time intervals.

on the hydrogen abstraction from the electrolyte solvent (diglyme) can be proposed to explain the formation of the oxalate-based side products:[27]

Methyl H-abstraction:

$$C_6H_{14}O_3 \rightarrow 2CH_2O + C_4H_{10}O \quad (3)$$

$$2CH_2O + 2NaO_2 \rightarrow (H/Na)_2C_2O_4 + 2(Na/H)OH \quad (4)$$

In addition, methylene H-abstraction from diglyme has also been proposed to result in formation of methoxy (oxo)acetic anhydride by Black et al:[27]

$$C_6H_{14}O_3 + 4NaO_2 \rightarrow C_6H_6O_7 + 4NaOH + 2H_2 \quad (5)$$

The resultant anhydride on NaO_2 may react with water from eq 4 to form methyl oxalate:

$$C_6H_6O_7 + H_2O \rightarrow 2C_3H_4O_4 \quad (6)$$

It should be noted that methyl oxalate also exhibits a strong peak related to CH_3−O stretching mode at 860−870 cm^{-1}.[28] The proposed reaction mechanisms are also summarized in Figure 4.

Thus, the spectroscopic evidence illustrates that oxalate-based side products are mainly formed on the NaO_2 discharge

DOI: 10.1021/acs.chemmater.8b01704
Chem. Mater. XXXX, XXX, XXX−XXX

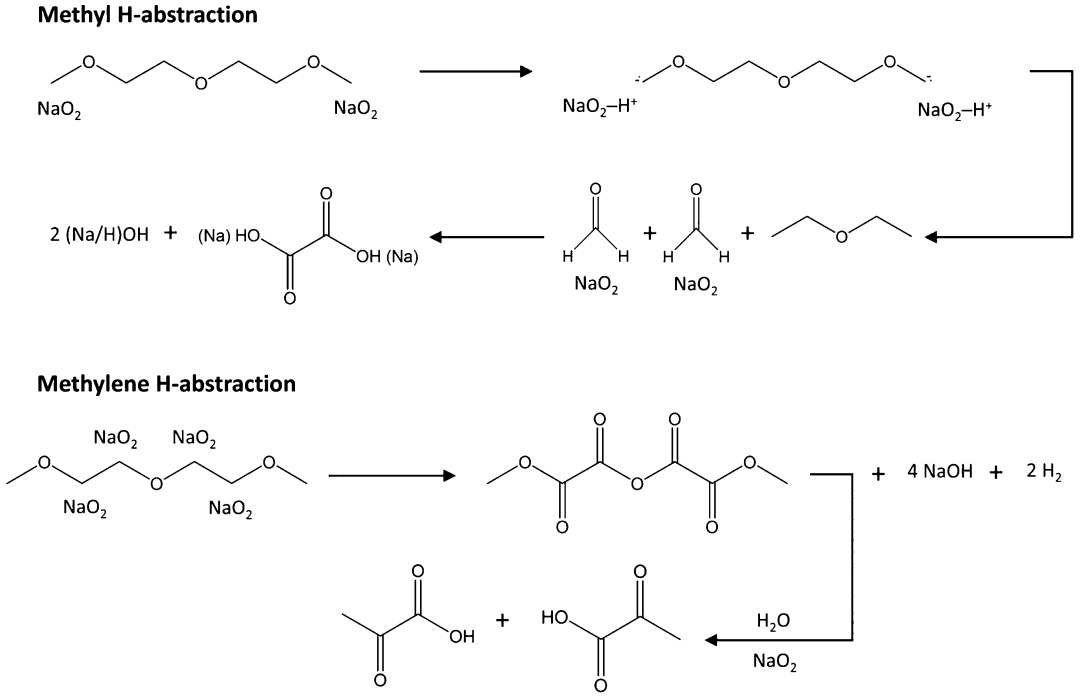

Figure 4. Proposed reaction mechanisms for decomposition of diglyme on NaO_2 surface and formation of oxalate-based side products.

product of the cell on rest. Moreover, appearance of the peak at 1136 cm^{-1} (Figure 3) can be correlated to the NaO_2 phase in the (Na/H)OH environment based on the proposed mechanism. The increased antibonding electron density on O_2^- results in decreased bond order and appearance of the lower frequency peak. This can be further confirmed by the disappearance of the peak due to the decomposition of NaO_2 at the surface or consumption of (Na/H)OH in the subsequent reactions. It is noteworthy that the total decomposition of NaO_2 cannot be concluded based on the disappearance of the surface-sensitive Raman signals. Meantime, the obtained results contradict with formation of $Na_2O_2 \cdot 2H_2O$ proposed mainly based on XRD data.[17−19] Nevertheless, decomposition of NaO_2 by high-energy X-ray beam cannot be ruled out. To examine the hypothesis, a discharged air electrode was placed in an airtight XRD holder and subjected to consecutive scans with different time intervals (Figure S12). Most of NaO_2 content was maintained unchanged during the first 15 h under XRD scans with longer intervals, whereas the majority of NaO_2 was converted to $Na_2O_2 \cdot 2H_2O$ during the second 12 h scans with shorter intervals. Therefore, precautions should be taken when applying high-energy probes to Na−O_2 cells.

The results obtained in this study further support our recent in situ XAS study on discharge/charge reaction mechanism of Na−O_2 cells.[16] Compared to XAS technique, however, Raman demonstrates higher selectivity toward the potential organic side products forming as a result of solvent decomposition (see also Figure S5). In addition, the low-energy probe used in Raman to provide analytical information makes it a very useful tool for studying the reactions occurring at the products/electrolyte interfaces. Moreover, the obtained results are also consistent with the findings from conventional analytical methods.[27] Nevertheless, Raman imaging technique enables in situ monitoring of the reactions at the NaO_2/electrolyte interface without any potential interferences from external contamination sources.

In summary, the presented results demonstrate the capability of Raman spectroscopy to study the reaction mechanisms in Na−O_2 cells. The combination of visual inspection with chemical imaging techniques provides a unique tool to acquire detailed information about the underlying mechanism of the cell. In addition, the low-energy probe in the visible range of the spectrum used by Raman spectroscopy eliminates the potential source of uncertainty caused by the measuring technique. Our preliminary in situ study on the decomposition reaction of NaO_2 revealed that oxalate-based side products are formed by exposing the discharge product to the cell electrolyte over a prolonged period of time. Moreover, carbonate-based side products were found to form on the carbonaceous air electrode on discharge. In-operando Raman studies are expected to reveal more details about the electrochemical reaction mechanism of the cell which are currently ongoing in our group.

■ ASSOCIATED CONTENT

Supporting Information

The Supporting Information is available free of charge on the ACS Publications website at DOI: 10.1021/acs.chemmater.8b01704.

Digital and SEM images, reference Raman spectra, additional chemical maps, and XRD spectra (PDF)

■ AUTHOR INFORMATION

Corresponding Author

*E-mail: xsun@eng.uwo.ca.

ORCID

Hossein Yadegari: 0000-0002-2572-182X

Mohammad Norouzi Banis: 0000-0002-6144-6837

Xueliang Sun: 0000-0003-2881-8237

Notes

The authors declare no competing financial interest.

DOI: 10.1021/acs.chemmater.8b01704
Chem. Mater. XXXX, XXX, XXX−XXX

■ ACKNOWLEDGMENTS

This research was supported by Natural Sciences and Engineering Research Council of Canada, Canada Research Chair Program, Canada Foundation for Innovation, and the University of Western Ontario.

■ REFERENCES

(1) Luntz, A. C.; McCloskey, B. D. Nonaqueous Li-Air Batteries: A Status Report. *Chem. Rev.* **2014**, *114*, 11721−11750.
(2) Aurbach, D.; McCloskey, B. D.; Nazar, L. F.; Bruce, P. G. Advances in understanding mechanisms underpinning lithium-air batteries. *Nat. Energy* **2016**, *1*, 16128.
(3) Hartmann, P.; Bender, C. L.; Vracar, M.; Durr, A. K.; Garsuch, A.; Janek, J.; Adelhelm, P. A rechargeable room-temperature sodium superoxide (NaO_2) battery. *Nat. Mater.* **2013**, *12*, 228−232.
(4) Xia, C.; Black, R.; Fernandes, R.; Adams, B.; Nazar, L. F. The critical role of phase-transfer catalysis in aprotic sodium oxygen batteries. *Nat. Chem.* **2015**, *7*, 496−501.
(5) McCloskey, B. D.; Speidel, A.; Scheffler, R.; Miller, D. C.; Viswanathan, V.; Hummelshoj, J. S.; Norskov, J. K.; Luntz, A. C. Twin Problems of Interfacial Carbonate Formation in Nonaqueous Li-O_2 Batteries. *J. Phys. Chem. Lett.* **2012**, *3*, 997−1001.
(6) Thotiyl, M. M. O.; Freunberger, S. A.; Peng, Z. Q.; Bruce, P. G. The Carbon Electrode in Nonaqueous Li-O_2 Cells. *J. Am. Chem. Soc.* **2013**, *135*, 494−500.
(7) Yadegari, H.; Sun, Q.; Sun, X. Sodium-Oxygen Batteries: A Comparative Review from Chemical and Electrochemical Fundamentals to Future Perspective. *Adv. Mater.* **2016**, *28*, 7065−7093.
(8) McCloskey, B. D.; Garcia, J. M.; Luntz, A. C. Chemical and Electrochemical Differences in Nonaqueous Li-O_2 and Na-O_2 Batteries. *J. Phys. Chem. Lett.* **2014**, *5*, 1230−1235.
(9) Yadegari, H.; Banis, M. N.; Xiao, B.; Sun, Q.; Li, X.; Lushington, A.; Wang, B.; Li, R.; Sham, T.-K.; Cui, X.; Sun, X. Three-Dimensional Nanostructured Air Electrode for Sodium-Oxygen Batteries: A Mechanism Study toward the Cyclability of the Cell. *Chem. Mater.* **2015**, *27*, 3040−3047.
(10) Yadegari, H.; Sun, X. Recent Advances on Sodium-Oxygen Batteries: A Chemical Perspective. *Acc. Chem. Res.* **2018**, *51*, 1532−1540.
(11) Zhao, Y.; Goncharova, L. V.; Zhang, Q.; Kaghazchi, P.; Sun, Q.; Lushington, A.; Wang, B. Q.; Li, R. Y.; Sun, X. L. Inorganic-Organic Coating via Molecular Layer Deposition Enables Long Life Sodium Metal Anode. *Nano Lett.* **2017**, *17*, 5653−5659.
(12) Zhao, Y.; Goncharova, L. V.; Lushington, A.; Sun, Q.; Yadegari, H.; Wang, B. Q.; Xiao, W.; Li, R. Y.; Sun, X. L. Superior Stable and Long Life Sodium Metal Anodes Achieved by Atomic Layer Deposition. *Adv. Mater.* **2017**, *29*, 1606663.
(13) Reeve, Z. E.; Franko, C. J.; Harris, K. J.; Yadegari, H.; Sun, X.; Goward, G. R. Detection of Electrochemical Reaction Products from the Sodium-Oxygen Cell with Solid-State ^{23}Na NMR Spectroscopy. *J. Am. Chem. Soc.* **2017**, *139*, 595−598.
(14) Landa-Medrano, I.; Sorrentino, A.; Stievano, L.; Ruiz de Larramendi, I.; Pereiro, E.; Lezama, L.; Rojo, T.; Tonti, D. Architecture of Na-O_2 battery deposits revealed by transmission X-ray microscopy. *Nano Energy* **2017**, *37*, 224−231.
(15) Sayed, S. Y.; Yao, K. P.; Kwabi, D. G.; Batcho, T. P.; Amanchukwu, C. V.; Feng, S.; Thompson, C. V.; Shao-Horn, Y. Revealing instability and irreversibility in nonaqueous sodium-O_2 battery chemistry. *Chem. Commun.* **2016**, *52*, 9691−9694.
(16) Banis, M. N.; Yadegari, H.; Sun, Q.; Regier, T.; Boyko, T.; Zhou, J.; Yiu, Y. M.; Li, R.; Hu, Y.; Sham, T. K.; Sun, X. Revealing the charge/discharge mechanism of Na-O_2 cells by in situ soft X-ray absorption spectroscopy. *Energy Environ. Sci.* **2018**, DOI: 10.1039/C8EE00721G.
(17) Yadegari, H.; Franko, C. J.; Banis, M. N.; Sun, Q.; Li, R.; Goward, G. R.; Sun, X. How to Control the Discharge Products in Na-O_2 Cells: Direct Evidence toward the Role of Functional Groups at the Air Electrode Surface. *J. Phys. Chem. Lett.* **2017**, *8*, 4794−4800.
(18) Kim, J.; Park, H.; Lee, B.; Seong, W. M.; Lim, H. D.; Bae, Y.; Kim, H.; Kim, W. K.; Ryu, K. H.; Kang, K. Dissolution and ionization of sodium superoxide in sodium-oxygen batteries. *Nat. Commun.* **2016**, *7*, 10670.
(19) Ortiz-Vitoriano, N.; Batcho, T. P.; Kwabi, D. G.; Han, B.; Pour, N.; Yao, K. P. C.; Thompson, C. V.; Shao-Horn, Y. Rate-Dependent Nucleation and Growth of NaO_2 in Na-O_2 Batteries. *J. Phys. Chem. Lett.* **2015**, *6*, 2636−2643.
(20) Vacque, V.; Sombret, B.; Huvenne, J. P.; Legrand, P.; Suc, S. Characterisation of the O-O peroxide bond by vibrational spectroscopy. *Spectrochim. Acta, Part A* **1997**, *53*, 55−66.
(21) Rolfe, J.; Holzer, W.; Murphy, W. F.; Bernstein, H. J. Some Spectroscopic Constants for O_2^- Ions in Alkali Halide Crystals. *J. Chem. Phys.* **1968**, *49*, 963.
(22) Creighton, J. A.; Lippincott, E. R. Vibrational Frequency and Dissociation Energy of Superoxide Ion. *J. Chem. Phys.* **1964**, *40*, 1779−1780.
(23) Oliver, B. G.; Davis, A. R. Vibrational Spectroscopic Studies of Aqueous Alkali-Metal Bicarbonate and Carbonate Solutions. *Can. J. Chem.* **1973**, *51*, 698−702.
(24) Miles, M. G.; Doyle, G.; Cooney, R. P.; Tobias, R. S. Raman and Infrared Spectra and Normal Coordinates of Trifluoromethanesulfonate and Trichloromethanesulfonate Anions. *Spectrochim. Acta Part A* **1969**, *25*, 1515−1526.
(25) Edwards, H. G. M.; Lewis, I. R. Ft-Raman Spectroscopic Studies of Metal Oxalates and Their Mixtures. *Spectrochim. Acta Part A* **1994**, *50*, 1891−1898.
(26) Jeziorowski, H.; Moser, B. Raman-Spectroscopic Studies of the Interaction of Oxalic-Acid and Sodium Oxalate Used as Corrosion-Inhibitors with Copper. *Chem. Phys. Lett.* **1985**, *120*, 41−44.
(27) Black, R.; Shyamsunder, A.; Adeli, P.; Kundu, D.; Murphy, G. K.; Nazar, L. F. The Nature and Impact of Side Reactions in Glyme-based Sodium-Oxygen Batteries. *ChemSusChem* **2016**, *9*, 1795−1803.
(28) Durig, J. R.; Brown, S. C. Vibrational-Spectra and Structure of Dimethyl Oxalate and Dimethyl Oxalate-D6. *J. Mol. Struct.* **1976**, *31*, 11−21.

DOI: 10.1021/acs.chemmater.8b01704
Chem. Mater. XXXX, XXX, XXX−XXX